Materials Research. 2018; 21(4): e20171077
DOI: http://dx.doi.org/10.1590/1980-5373-MR-2017-1077

Structural, Thermal, Optical, and Photoacoustic Study of Mechanically Alloyed Nanocrystalline SnTe

Zeane Vieira Borges[a], Claudio Michel Poffo[b], João Cardoso de Lima[c]*, Sérgio Michielon de Souza[d], Daniela Menegon Trichês[d], Ronaldo Sérgio de Biasi[e]

[a]Departamento de Engenharia Mecânica, Universidade Federal de Santa Catarina, Campus Universitário Trindade, C.P. 476, 88040-900, Florianópolis, SC, Brasil
[b]Coordenadoria Especial de Física, Química e Matemática, Universidade Federal de Santa Catarina, Campus Araranguá, 88900-000, Araranguá, SC, Brasil
[c]Departamento de Física, Universidade Federal de Santa Catarina, Campus Trindade, C.P. 476, 88040-900, Florianópolis, SC, Brasil
[d]Departamento de Física, Instituto de Ciências Exatas, Universidade Federal do Amazonas, 69077-000, Manaus, AM, Brasil
[e]Seção de Engenharia Mecânica e de Materiais, Instituto Militar de Engenharia, 22290-270, Rio de Janeiro, RJ, Brasil

Received: December 08, 2017; Revised: April 03, 2018; Accepted: April 15, 2018

A nanostructured SnTe phase was produced by mechanical alloying after 2 h of milling. Part of the as-milled powder was annealed and its X-ray diffraction (XRD) pattern was recorded. The XRD patterns of the as-milled and annealed samples were refined using the Rietveld method. After annealing, partial decomposition of the SnTe phase was observed and corroborated by estimating the mean crystallite size using a Willianson-Hall plot. The Cowley-Warren parameter α_{SnTe}^{CW} for the first coordination shell was calculated, showing a preference for homopolar pairs. This preference is consistent with the partial decomposition observed. According to the optical absorbance spectra, the band gap energy is inversely proportional to crystallite size, following a decaying exponential function. From the photoacoustic absorption spectroscopy measurements, the thermal diffusivity parameter and the transport properties of as-milled and annealed SnTe powder were determined.

Keywords: *Semiconductors, Nanocrystals, Mechanical alloying, Thermoelectric materials, X-ray diffraction, Photoacoustic absorption spectroscopy.*

1. Introduction

Chalcogenide semiconductor compounds are of considerable interest due to their optical[1], electronic[2], and optoelectronic[3] applications. In particular, the tin telluride (SnTe) compound has potential applications in mid-infrared (3-14 μm) detection and thermoelectric conversion[4-7].

According to the Inorganic Crystal Structure Database (ICSD)[8], code 188457, at room temperature and atmospheric pressure, the SnTe compound crystallizes in a cubic structure (S.G. Fm3-m, Z = 4), with the Sn atoms occupying the Wyckoff site 4*a* (0, 0, 0) and the Te atoms occupying the site 4*b* (0.5, 0.5, 0.5). This compound can be synthesized using the techniques of molecular beam epitaxy[9], electrodeposition[10], solution-phase synthesis[11] and mechanical alloying (MA)[12,13]. MA has been used for synthesizing crystalline compounds, amorphous materials and solid solutions[14-17]. It has also been used to produce nanostructured materials as well as alloys whose components have large differences in their melting points, making difficult their production through techniques based on fusion[18].

Nanostructured materials are metastable and can be described by two structural components, one containing crystallites with nanometer dimensions (2-100 nm), that have the same structure as the bulk crystalline counterpart, and an interfacial component formed by different kinds of defects (grain boundaries, interphase boundaries, dislocations, etc.)[19]. Commonly, the volume fractions of the two components are of the same order, leading a strong dependence of the material properties on the atomic arrangements of the interfacial phase[19]. Manipulation of these atomic arrangements leads to the possibility of designing new materials with the properties required for specific technological applications[20].

Since MA yields materials containing a high concentration of defect centers, it is interesting to investigate the influence of concentration of defect centers on the structural, optical, thermal, and photoacoustic properties of SnTe. For this, the X-ray diffraction (XRD), differential scanning calorimetry (DSC), optical absorbance (UV-VIS-NIR), and photoacoustic absorption spectroscopy (PAS) techniques were used. This paper reports the results obtained for as-milled and annealed nanostructured SnTe.

*e-mail: joao.cardoso.lima@ufsc.br

2. Determination of mean crystallite size and strain using the Williamson-Hall plot and a pseudo-Voigt function to describe the diffraction line profiles

The diffraction line broadening is well described by a Voigt function, which is described by a convolution of Gaussian and Lorentzian (also called as Cauchy) functions. In a single line analysis, the apparent crystallite size is calculated using the Scherrer formula[21] $D = \frac{0.91\lambda}{\beta_L \cos\theta}$ and the strain is calculated using the formula[22] $\sigma_p = \frac{\beta_G}{4\tan\theta}$ where θ is the diffraction angle, λ is the X-ray wavelength and β_L and β_G are the Lorentzian and Gaussian integral breadths of the diffraction line. The β_L and β_G integral breadths are related to full widths at half maximum (FWHM) of the normalized Lorentzian Γ_L and Gaussian Γ_G components by the expressions $\beta_L = \frac{\pi}{2}\Gamma_L$ and $\beta_G = \frac{\Gamma_G}{2}\sqrt{\frac{\pi}{\ln 2}}$. The shape of the Voigt function is determined by the relative intensities of the two components. The pseudo-Voigt function, $pV(x)$, is an approximation of the Voigt function that substitutes the shape parameters Γ_L and Γ_G by two other parameters, Γ and η. The function is a linear combination of Lorentzian and Gaussian functions with the same FWHM, Γ, and a parameter $0.328^{23} \leq \eta \leq 1$ used to specify the relative intensity of the Lorentzian component.

The relations between the Γ_G and Gaussian Γ_L of the Voigt function and the Γ and η of $pV(x)$ are given by the expressions,

$$\Gamma_G = (1 - 0.74417\eta - 0.24781\eta^2 - 0.00810\eta^3)^{1/2}\Gamma = c_1\Gamma \quad (1)$$

and

$$\Gamma_L = (0.72928\eta + 0.19289\eta^2 + 0.07783\eta^3)\Gamma = c_2\Gamma \quad (2)$$

Using the relations $\beta_G = \frac{\Gamma_G}{2}\sqrt{\frac{\pi}{\ln 2}} = c_1 c_3 \Gamma$ and $\beta_L = \frac{\pi}{2}\Gamma_L = c_2 c_4 \Gamma$, where $c_3 = \frac{1}{2}\sqrt{\frac{\pi}{\ln 2}}$ and $c_4 = \frac{\pi}{2}$, we have $\beta_L + \beta_G = (c_1 c_3 + c_2 c_4)\Gamma$

$$\frac{091\lambda}{D\cos\theta} + 4\sigma_P \tan\theta = (c_1 c_3 + c_2 c_4)\Gamma \quad (3)$$

or

$$\Gamma\cos\theta = \frac{0.91\lambda}{D(c_1 c_3 + c_2 c_4)} + \frac{4\sigma_P}{(c_1 c_3 + c_2 c_4)}\sin\theta \quad (4)$$

Expression (4) is the standard equation for a straight line ($y = a + bx$). By plotting $\Gamma\cos\theta$ versus $\sin\theta$ we obtain the mean microstrain component from the slope and the mean crystallite size from the interception with the $\Gamma\cos\theta$ axis. Such plot is known as the Williamson-Hall plot. The Γ and η values are obtained directly from the Rietveld refinement of the XRD pattern.

A relationship between the crystallite size D and the microstrain σ_p can be obtained due to the fact that $pV(x)$ is a linear combination of Lorentzian and Gaussian functions with the same FWHM (Γ), and

$$D\sigma_p = \frac{0.91\lambda c_1 c_3}{4c_2 c_4 \sin\theta} \quad (5)$$

Eq. (5) should be used in a single line analysis only, i.e., after determining the apparent crystallite size.

3. Experimental Procedure

High-purity elemental powders of tin (Alfa Aesar 99.8 %) and tellurium (Alfa Aesar 99.999 %) were blended with SnTe nominal composition was sealed together with several steel balls of 1.5 cm in diameter into a cylindrical steel vial under argon atmosphere. The ball-to-powder weight ratio was 5:1. MA was performed using an 8000 Spex Mixer/Mill at room temperature, and a ventilation system was used to keep the vial temperature close to room temperature. The milling process was stopped after 2 h when the XRD pattern of the as-milled powder showed an excellent agreement with the pattern given in the ICSD code 188457 for the SnTe phase[8]. The XRD patterns were recorded using a Philips X-Pert powder diffractometer, using the Cu Kα radiation (λ = 1.5406 Å). The XRD patterns were refined using the Rietveld method[24], implemented in the GSAS package[25]. The XRD pattern of a certified elemental silicon sample was recorded in the same experimental conditions and used to take into account the instrumental broadening for the Rietveld refinements. A $pV(x)$ function was used to describe the diffraction lines profiles. Thermal parameter (Uiso) was assumed to be isotropic.

The thermal stability of the SnTe phase was investigated using DSC measurements from room temperature up to 500 ºC, with a heating rate of 10 ºCmin^{-1}, under nitrogen flow, using Al pans in a TA Instruments 2010 DSC cell. Based on the thermograms, annealing was carried out on a portion of the as-milled SnTe powder in order to study the influence of concentration of the defect centers on the properties previously mentioned. For this, a pellet of SnTe was inserted into an evacuated quartz tube, which was maintained under low pressure (≈ 10^{-3} Torr) in argon gas. The sample was annealed at 320 ºC for 2.5 h, followed by air cooling.

The optical properties of the as-milled and annealed nanostructured SnTe samples were studied using UV-VIS-NIR measurements. The optical transmittance measurements were taken in an energy range of 0.06-0.50 eV, using a Perkin-Elmer FT-IR Spectrometer, Spectrum 100. For measurements, as-milled and annealed powders were dispersed into KBr powder and pressed using the same pressure to form pellets.

The PAS measurements were carried out in an open photoacoustic cell (OPC) setup built at home. Details about the OPC setup can be found in Refs. 26 and 27. The samples for the OPC measurements were prepared by compressing at the same pressure (6 tons) the as-milled and annealed SnTe powders to form tiny circular pellets, 10 mm in diameter, with thickness of 440 μm and 450 μm, respectively. The samples were mounted

directly onto the front sound inlet of an electret microphone, and periodically illuminated to generate the photoacoustic effects, as described by the thermal diffusion model.

4. Results and Discussion

4.1 XRD and DSC measurements

Figure 1 shows the XRD pattern (black open circles) recorded for 2 h of milling. It was compared with those given in the ICSD Database[8] for the Sn-Te system, and an excellent agreement was observed with that for cubic SnTe (ICSD code No. 188457). Besides the diffraction peaks of SnTe, two low intensity diffraction peaks at about 2θ = 27º and 34º were observed, and indexed to SnO_2 (ICSD code 9163). The SnO_2 peaks did not appear in the XRD patterns of the Sn and Te powders used to prepare the samples. Then, its nucleation probably occurred during manipulation of the powder to perform the XRD measurements and is probably restricted to the region close to the particle surface. The enthalpies for formation of the SnO_2, TeO_2, and SnTe phases are -596.429 kJ/mol, -345.503 kJ/mol, and -91.737 kJ/mol[28], respectively.

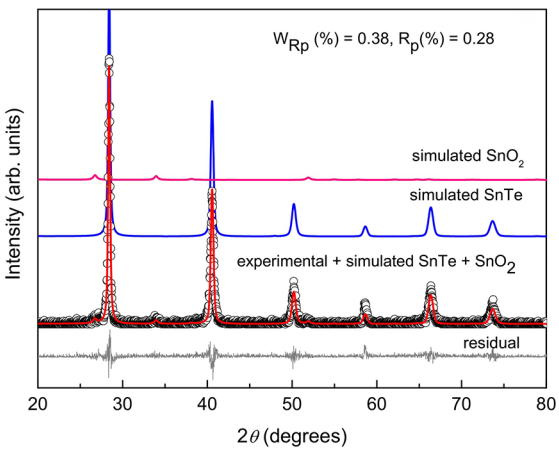

Figure 1. (color online): Experimental and simulated XRD patterns of an as-milled SnTe sample after 2 h of milling. The simulated SnTe and SnO_2 phases as well as the difference between experimental and simulated patterns (bottom line) are also shown

For the Rietveld refinement of the XRD pattern of the as-milled sample, shown in Fig. 1, the structural models in the ICSD codes for SnTe and SnO_2 given above were used. The best fit was reached for the lattice parameters a = 6.3183 Å (6.3183 Å), η = 0.328 for SnTe and $a = b$ = 4.7333 Å (4.7380 Å), c = 3.1971 Å (3.1865 Å), η = 0.328 for SnO_2. The values within parentheses are those given in the ICSD codes above. The thermal parameter (Uiso) was assumed to be isotropic. The simulated XRD patterns for the as-milled sample as well as the individual patterns for SnTe and SnO_2 and the difference between experimental and simulated patterns (bottom line) are shown in Fig. 1, from where one can see an excellent agreement.

The Rietveld refinement does not take into account the contribution of the background to calculate the relative volume fractions of phases composing the experimental XRD pattern. The relative volume fractions were 96 % for SnTe and 4 % for SnO_2. The goodness-of-fit indicators R_p and R_{wp} are shown in this figure.

The XRD pattern of as-milled samples shows broad peaks, suggesting that the mean crystallite size D of the SnTe phase is of nanometer dimension. The values of D and of the microstrain σ_p were estimated through the Williamson-Hall plot, using a pseudo-Voigt function to describe the profiles of peaks in the Rietveld refinement, as shown in Section 2. The values of Γ and θ were obtained from the Rietveld refinement. Figure 2 shows the Γ cos θ *vs* sin θ data for the SnTe phase. By fitting the data to a straight line, values of D = 75.2 nm and of σ_p = 0.45 % were obtained.

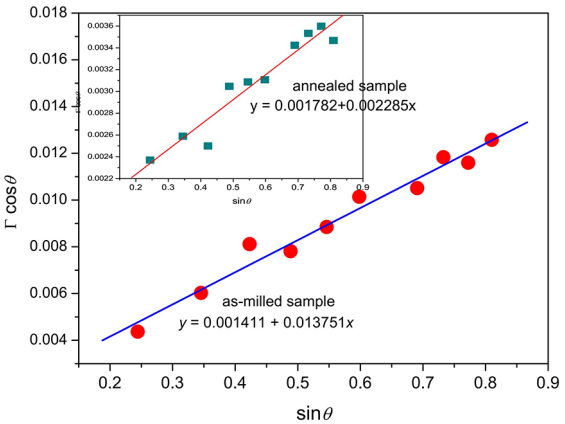

Figure 2. (color online): Willianson-Hall plot for the as-milled and annealed (inset) SnTe samples

As described in the Section 3, part of the as-milled SnTe powder was annealed in order to study the influence of concentration of the defect centers on the properties previously mentioned. Figure 3 shows the XRD pattern of the annealed sample. The pattern shows, besides the peaks of SnTe and SnO_2, low intensity peaks at about 2θ = 27.6º and 38.3º that were indexed to elemental Te (ICSD code 65692)[8]. The best Rietveld refinement of this XRD pattern was reached considering the values of lattice parameter a = 6.3155 Å, η = 0.328 for SnTe; $a = b$ = 4.7390 Å, c = 3.1907 Å, η = 0.328 for SnO_2; and $a = b$ = 4.4718 Å (4.456 Å), c = 5.9167 Å (5.921 Å), η = 0.328 for elemental Te. The values within parentheses are those given in the ICSD code 65692. The simulated XRD patterns for the annealed sample and individual patterns for SnTe, SnO_2, elemental Te, and the difference between experimental and simulated patterns (bottom line) are shown in Fig. 3, from where one can see an excellent agreement. The relative volume fractions were 77 % for SnTe, 13 % for SnO_2, and 10 % for elemental Te. It is

interesting to note that after annealing, the volume fraction of SnTe decreased 19 % and the volume fraction of SnO_2 increased 9 %. The goodness-of-fit indicators R_p and R_{wp} are shown in this figure.

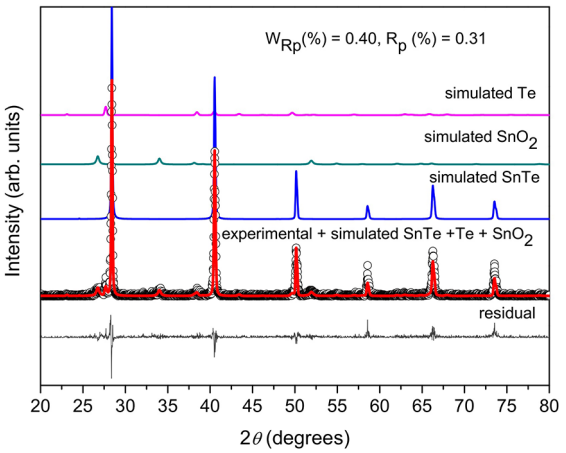

Figure 3. (color online): Experimental and simulated XRD patterns of an annealed SnTe sample. The simulated SnTe, SnO_2 and elemental Te phases as well as the difference between experimental and simulated patterns (bottom line) are also shown

As for as-milled SnTe, the values of D and σ_p for annealed SnTe were estimated using the Williamson-Hall plot, which is shown in the inset of Fig. 2. By fitting to a straight line, values of D = 59.3 nm and σ_p = 0.075 % were obtained. It is interesting to note that, after annealing, a variation of ≈ 21% in the mean crystallite size is observed, and this value is close to the variation in the volume fraction of SnTe (19 %).

Chemical disorder is among the physical mechanisms responsible for phase transformation, amorphization and decomposition of alloys with increasing pressure and/or temperature, but it has not received the attention it deserves. Trying to explain the partial decomposition of nanostructured SnTe under annealing, the influence of chemical disorder was investigated. The Cowley-Warren chemical short-range order (CSRO) parameter α^{CW}, used to study the statistical distribution of atoms in solids, is given by[29]

$$\alpha_{ij}^{CW} = 1.0 - \frac{N_{ij}}{c_j\left[c_j\left(N_{ii}+N_{ij}\right)+c_i\left(N_{jj}+N_{ji}\right)\right]}, \quad (6)$$

where N_{ii}, N_{ij} and N_{jj} are the coordination numbers and c_i and c_j are the concentrations of atoms of the elements i and j. The α^{CW} parameter is zero for a random distribution, negative if there is a preference for forming unlike pairs and positive if homopolar pairs (clusters or local order) are preferred. Although the α^{CW} parameter is usually applied to amorphous phases, it can also be used to determine the relative preference for forming different atomic pairs and thus to investigate the crystallization behavior of a binary alloy. The coordination numbers N_{SnSn}, N_{SnTe}, N_{TeSn} and N_{TeTe} were obtained using the structural data given in ICSD 188457 for SnTe in the Crystal Office 98 software[30] to build the 3D structure, and using the tool "shell structure" the R_{SnSn}, R_{SnTe}, and R_{TeTe} interatomic distances were calculated up to 10 Å. By putting the origin at Sn atoms (site 4*a*), the coordination numbers for the first neighbors are N_{SnSn} = 12 at 4.4670 Å and N_{SnTe} = 6 at 3.1590 Å. By putting the origin at Te atoms (site 4*b*), the coordination numbers for the first neighbors are N_{TeSn} = 6 at 3.1590 Å and N_{TeTe} = 12 at 4.4675 Å. Using the values in Eq. (6), a value of α_{SnTe}^{CW} = 0.333 is obtained, indicating a preference for forming homopolar pairs in the first coordination shell. This value suggests that the repulsive part of the crystalline field plays an important role in the structural stability of this phase. During annealing, the thermal movements of the Sn and Te atoms may be responsible for introducing structural instability, promoting the partial decomposition of SnTe.

In order to understand the partial decomposition of the SnTe phase under annealing, part of as-milled powder was studied using DSC measurements. Figure 4 shows two sequentially recorded DSC thermograms for the same as-milled sample, and one run for the annealed sample, with a heating rate of 10 ºC min^{-1} under nitrogen flow. In the first run (blue top line), one can see an exothermic peak at about 278 ºC and a low intensity exothermic broad band between 384 ºC and 417 ºC. In the second run (black middle line) one can see the previous exothermic peak slightly shifted toward lower temperatures (≈ 265 ºC), and an endothermic peak at about 392 ºC. In the thermogram for the annealed sample (red bottom line), one can see the previous exothermic peak shifted toward higher temperatures(≈ 291 ºC) and the endothermic peak at about 395 ºC, now well-defined and seeming to be formed by two endothermic peaks (see inset).

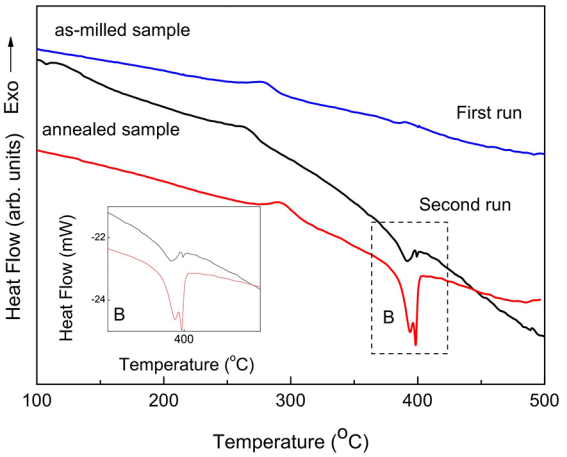

Figure 4. (color online): DSC thermograms of the as-milled and annealed samples

In order to analyze the DSC thermograms shown in Fig. 4, the following values of the melting points (T_m) are useful: 232.08 ºC for Sn, 449.6 ºC for Te, 806 ºC for SnTe, 1080 ºC for SnO, 1727 ºC forSnO_2,

733 ºC for TeO_2, and 430 ºC for TeO_3. Based on these values, one can see that the endothermic peak at about 395 ºC cannot be associated with the fusion of any of the phases above. Youngku Sohn[31] investigated the formation of SnO_2 starting from the decomposition a Sn-polymer complex. The TG/DSC thermogram shown in Fig. 4 (right) of Ref. 31 displays an endothermic peak at about 395 ºC, similar in shape and temperature to the endothermic peak observed in this study, that was attributed to formation of SnO_2. Only in the DSC thermograms of the as-milled (second run) and annealed samples this endothermic peak is observed. On the other hand, the XRD pattern of the annealed sample showed a decrease in the relative volume fraction of SnTe. Thus, we attribute the endothermic peak located between 390 ºC and 400 ºC to the formation of SnO_2 from Sn atoms originated from the partial decomposition of SnTe under annealing. With respect to the exothermic peak observed between 260 ºC and 295 ºC in the three thermograms, it can be associated with crystallization from an amorphous phase and/or with a phase transformation. No amorphous phase was observed in the XRD patterns of as-milled and annealed samples; if it exists, its intensity is too low to be separated from the background or from the contribution of the interfacial component (diffuse scattering) to the XRD pattern. Manzato *et al*.[32] synthesized SnO and SnO_2 by high-energy milling. In the thermogram shown in Fig. 5 of Ref. 32, two exothermic peaks located at about 195 ºC and 287 ºC were attributed to the formation of SnO and SnO_2, respectively. Thus, we attribute the exothermic peak located between 260 ºC and 295 ºC to formation of the SnO_2 phase starting from the relaxation of Sn atoms located in the interfacial component of SnTe. Formation of pure Te can be due to the diffusion of Te atoms located at the interfacial component and/or from the partial decomposition of SnTe.

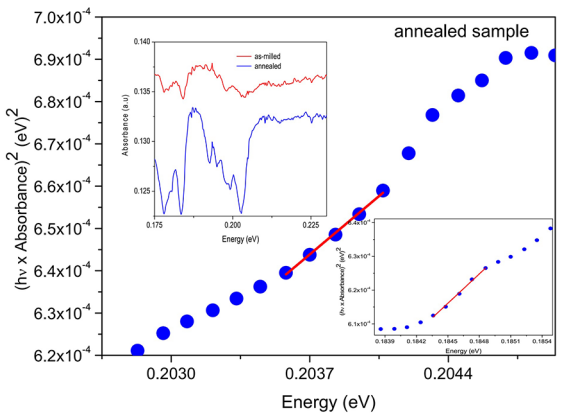

Figure 5. (color online): McLean plot for the as-milled SnTe sample (bottom inset), the annealed SnTe sample, and absorbance spectra for the as-milled and annealed SnTe samples (top inset)

4.2 Optical absorbance measurements

Commonly, the value of the optical band gap energy of a thin film is obtained by McLean analysis of the absorption edge[33]. Another way to obtain the optical band gap energy is presented in Ref. 34. The expression given in Ref. 33 was modified to be applied to a powder; the details are presented in Refs. 35,36 and will not be repeated here. The modified McLean equation is written in the form[35,36]

$$Ahv = l_s(hv - E_g + E_p)^{1/n} \qquad (7)$$

where A is the absorbance, h is the Planck constant, ν is the frequency of the incident beam, l_s is an adjustable parameter and n is an index representing the transition order. A value of $n = 2$ corresponds to a direct allowed transition, $n = 2/3$ to a direct forbidden transition, $n = 1/2$ to an indirect allowed transition and $n = 1/3$ to an indirect forbidden transition.

In this study, the transmittance data were converted to absorbance data using the expression $A = 2 - \log_{10}T$. Figure 5 shows the $(hv \times A)^2$ *vs* photon energy plot for the annealed sample and the inset (top) shows the absorbance *vs* photon energy plots for as-milled (red curve) and annealed (blue curve) samples. In the inset one can see that the optical absorption edge of the as-milled sample (red curve) is very broad due to the mean crystallite size of $D = 75.2$ nm and the microstrain of $\sigma_p = 0.45\%$, as well as the substantial interfacial component. These features hinder the precise determination of the optical band gap energy. On the other hand, the absorbance spectrum for the annealed SnTe sample (blue curve) shows a narrow optical absorption edge, despite decomposition of SnTe promoted by annealing, led to a reduction of the mean crystallite size (D = 59.3 nm). According to the Refs. 37 and 38, SnTe has a direct optical band gap (n = 2). Fitting of experimental data to the McLean equation (red straight line) yields a band gap energy of $E_g = 0.187$ eV.

It is interesting to compare the band gap energy for the annealed SnTe sample obtained in this study with other values reported in the literature. Ref. 38 reported a value of $E_g = 0.54$ eV for nanocrystals SnTe with dimension of 6.5 nm; Ref. 37 reported values of $E_g = 0.54$ eV and 0.39 eV for nanocrystals SnTe with dimensions of 7.2 nm and 14 nm, respectively; Refs. 38 and 39 reported a value of $E_g = 0.18$ eV for bulk SnTe ($D \geq 100$ nm) at room temperature. Figure 6 shows E_g *vs* D data above fitted to an exponential function $E_g = y_0 + A^* e^{(-D/B)}$. This figure suggests that the band gap energy is inversely proportional to the crystallite size and follows an exponential law. Assuming that this behavior is true, the mean crystallite size $D = 75.2$ nm of as-milled sample leads to a value of $E_g \approx 0.182$ eV. By fixing this value, a fitting of experimental data to the McLean equation (red straight line)

is shown in the inset (bottom) of Fig. 5. A brief theoretical explanation for the behavior observed above is the following: for any isolated X atom, for instance, semimetals (X = Si, Ge) or nonmetals (X = Se), the band gap is equal to the distance between the ground state and the first excited state. Due to the Pauli exclusion principle, both levels are broadened in a solid. This broadening leads to narrowing of the bandgap and, therefore, it is expected that the band gap in a solid be less than in an isolated atom[40]. In nanomaterials, the small number of atoms leads to a smaller interaction between atoms than in a bulk material. Thus, the energy levels are similar to those of isolated atoms. As the number of atoms decreases (i.e., as the volume of the nanomaterial decreases) the energy levels become more similar to those of isolated atoms[40]. A brief quantitative analysis is given by Z.G. Fthenakis[40].

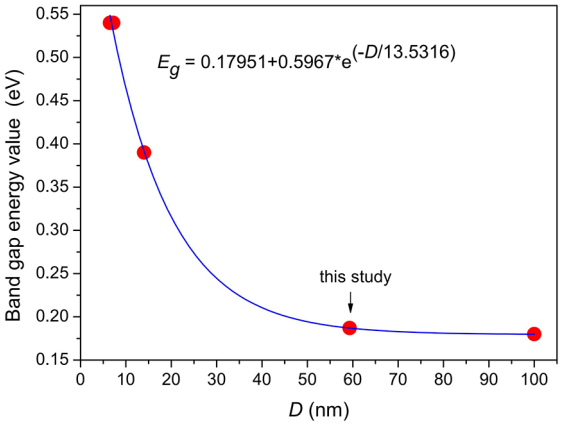

Figure 6. (color online): Mean crystallite size dependence of the optical band gap energy of SnTe.

4.3 PAS measurements

The determination of the thermal diffusivity parameter and/or the transport properties of semiconducting materials using PAS is widely documented in the literature. A theoretical summary of the PAS principles and applications are given in Refs. 41-47 and references therein and will not be repeated here.

The thermal diffusivity for bulk SnTe can be calculated using the expression for the thermal conductivity $k = \rho C_p \alpha$, where ρ is the density, C_p is the specific heat and α is the thermal diffusivity. The TAPP software (version 2.2)[28] gives values of $\rho = 6509$ kg.m^{-3} and $C_p = 211$ J kg^{-1}K^{-1} for SnTe. Gelbestein[48] reported a value of K = 7.9 Wm^{-1}K^{-1} for bulk SnTe. Using these values in the expression above, a value of $\alpha_{calc} = 0.0575$ x10^{-4} m^2 s^{-1} (0.0575 cm^2 s^{-1}) is obtained. Zhang *et al.*[49] produced an undoped SnTe phase and reported a value of $\alpha_{SnTe} = 0.056$ cm^2 s^{-1} for the thermal diffusivity at room temperature. The characteristic frequency $f_c = \alpha/\pi l_s^2$, where l_s is the sample thickness, is the modulation frequency corresponding to the transition from the thermally thin regime ($f < f_c$) to the thermally thick regime ($f > f_c$), where f is the modulation frequency. The thicknesses of the as-milled and annealed samples were 440 and 450 μm, yielding characteristic frequencies of 11.1 Hz and 10.6 Hz, respectively. The PAS data were acquired between 10 and 270 Hz to remain in the thermally thick regime.

Figure 7 shows the PAS signal amplitudes for as-milled and annealed SnTe and Fig. 8 shows the corresponding signal phases. According to Fig. 7, both signal amplitudes decrease with increasing modulation frequency. A similar behavior is observed in Fig. 8 for the signal phases. We used the procedure described in Ref. 44 to find the contribution of each heat transfer mechanism to the pressure variation in the photoacoustic cell and thus to take into account the contribution of intraband nonradiative thermalization (thermal diffusion). Figure 7 also shows that between 40 and 110 Hz and between 50 and 70 Hz, the PAS signal amplitudes for as-milled and annealed samples are proportional to $f^{-0.9807}$ and $f^{-0.9959}$, respectively, a behavior that may be attributed to nonradiative surface recombination, thermoelastic bending or thermal dilation[43,44,50]. Thermal dilation heat transfer mechanisms produce a signal whose phase is independent of the modulation frequency and equal to 90°. Since, according to Fig. 8, the signal phase decreases as the modulation frequency increases, this mechanism can be disregarded. The contribution of nonradiative bulk recombination heat transfer is proportional to $f^{-1.5}$. Usually, the phase of the photoacoustic signal corresponding to nonradiative bulk recombination exhibits a minimum that corresponds roughly to the point at which the phase dependence changes from $f^{-1.5}$ to $f^{-1.0}$, that is, it marks the transition from bulk to the surface recombination as the dominant mechanism responsible for the photoacoustic signal. This fact is discussed in Ref. 43. On the other hand, as reported by Dramicanin *et al.*[51], as the sample thickness decreases the minima in both amplitude and phase are shifted to higher frequencies and their intensities around this minimum decrease. It is interesting to note that the positions of these minima depend on the material investigated. By considering the results reported in Ref. 51 and the sample thicknesses used in this work, it is expected that these minima cannot be observed in the amplitude and phase PAS signals.

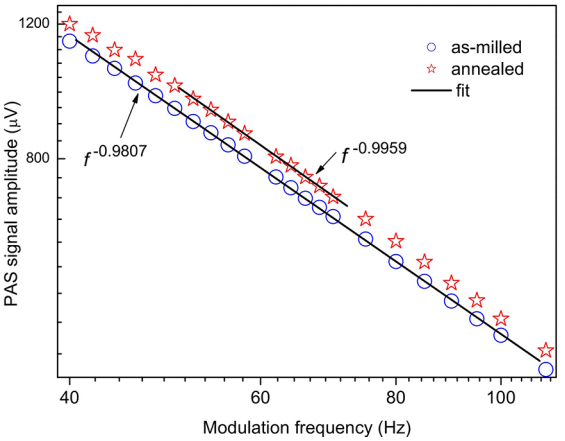

Figure 7. (color online): PAS signal amplitude vs modulation frequency for the as-milled (open circles) and annealed (open stars) samples. The solid lines are the best fits of the experimental data to straight lines

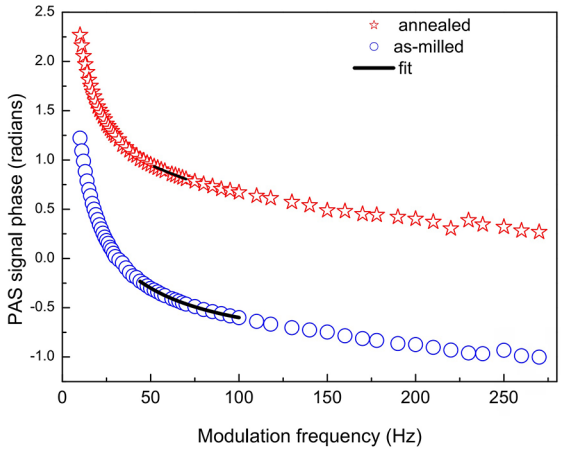

Figure 8. (color online): PAS signal phase vs modulation frequency for the as-milled (circles) and annealed (stars) samples. The solid lines are the best fits of the data for as-milled samples to Eq. (8) and of the data for annealed samples to Eq. (9).

In as-milled SnTe, the absence of the contribution of nonradiative bulk and surface recombination heat transfer mechanisms were verified by not being possible to fit the phase data to the phase expression given by Pinto Neto *et al.*[43] for these mechanisms, taking the thermal diffusivity value of α_{calc} = 0.0575 cm^2 s^{-1} as the initial value. On the other hand, the expression for the phase corresponding to the thermoelastic bending heat transfer mechanism[43-45] written as

$$\Phi_{ph} = \phi_0 + \tan^{-1}\left[\frac{1}{a\sqrt{f-1}}\right] \quad (8)$$

where $a = l_s\sqrt{\frac{\pi}{\alpha_s}}$, f *is* the modulation frequency, l_s is the sample thickness, and α_s its thermal diffusivity, was successfully fitted to the Φ_{ph} versus f plot in the modulation frequency range of 44-100 Hz. From the best fit, a value of α_{eff} = 0.0825 cm^2 s^{-1} was obtained for the thermal diffusivity. Similarly, in the annealed sample, the absence of the contribution of nonradiative bulk recombination and thermoelastic bending heat transfer mechanisms was verified by not being possible to fit the phase data to the phase expressions given in Refs. 43-45 for these mechanisms, taking the thermal diffusivity value of α_{calc} = 0.0575 cm^2 s^{-1} or 0.0825 cm^{2}s^{-1} as the initial value. On the other hand, the expression for the phase corresponding to nonradiative surface recombination heat transfer mechanism[43-45], written as

$$\Phi_{ph} = \frac{\pi}{2} + \tan^{-1}\left[\frac{(bD/v)(\omega\tau_{eff}+1)}{(bD/v)(1-\omega\tau_{eff}) - 1 - (\omega\tau_{eff})^2}\right] \quad (9)$$

where $\tau_{eff} = \tau(D/a - 1)$, $b = (\pi f/\alpha)^{1/2}$, $\omega = 2\pi f$, α is the termal diffusivity, D is the carrier diffusion coefficient, v is the surface recombination velocity and τ is the recombination time, was successfully fitted to the Φ_{ph} versus f plot in the modulation frequency range of 52-70 Hz. From the best fit, values of α_{eff} = 0.07305 cm^{2}s^{-1}, D = 29.82 cm^{2}s^{-1}, v = 149.94 cm s^{-1} and τ = 343.8 ns were obtained for the thermal diffusivity, carrier diffusion coefficient, surface recombination velocity and recombination time, respectively. The slight reduction in the thermal diffusivity for the annealed sample can be associated with decreasing the crystallite size and volume fraction of SnTe, accompanied by an increase in the volume fraction of SnO_2 and the emergence of a significant volume fraction of elemental Te. The last two phases can behave as phonon scattering centers, thus reducing the phonon free path.

It will be assumed that the measured effective thermal diffusivity α for as-milled and annealed samples can be described by the Lichtenecker's logarithmic mixture law[52,53]

$$\alpha_{eff} = \sum_i^n \alpha_i^{x_i} \quad (10)$$

where n is the number of phases and α_n and x_i are the thermal diffusivity and volume fraction of each phase, respectively. According to the Rietveld analysis, the relative volume fractions for the as-milled sample were 96% SnTe and 4% SnO_2, while for the annealed sample were 77% SnTe, 13 % SnO_2, and 10% elemental Te. The thermal diffusivity values of elemental Te[54] and SnO_2[28, 55] are α_{Te} = 0.0188 cm^{2}s^{-1} and α_{SnO2} = 0.3767 cm^{2}s^{-1}, respectively. Using the effective thermal diffusivity value of α_{eff} = 0.0825 cm^{2}s^{-1} for the as-milled sample and the relative volume fraction values above, a value of α_{SnTe} = 0.0774 cm^{2}s^{-1} is obtained for the as-milled SnTe phase, while a value of α_{SnTe} = 0.0660 cm^{2}s^{-1} is obtained for the annealed SnTe phase. These values are similar, but slightly larger than the value calculated using the TAPP data [28](α_{calc} = 0.0575 cm^2 s^{-1}). Using the high-energy ball milling and hot-pressing techniques, Zhang *et al.*[49] produced an undoped SnTe phase and reported a value of α_{SnTe} = 0.056 cm^2 s^{-1} for the thermal diffusivity at room temperature. This value agrees quite well with those obtained in this study.

The performance of a thermoelectric material can be improved if its thermal conductivity is reduced without strong degradation of the electrical properties. It has been reported that materials having small crystallite size can have larger thermoelectric conversion efficiency due a decrease in the thermal conductivity of the lattice[56, 57]. In this study, both as-milled and annealed samples have mean crystallite sizes of nanometric dimensions (75.2 nm and 59.3 nm).

According to Tripathi and Bhandari[58], the $\sqrt{Eg/K}$ ratio, where E_g is the energy gap in eV and K the thermal conductivity in W/mK, can be used as an initial guide to evaluate the good thermoelectric materials and gives a reasonably good agreement with the maximumvalue of ZT for these materials. The values of energy gap E_g = 0.182 eV for the as-milled and E_g = 0.187 eV for the annealed samples were obtained from the UV-VIS-NIR measurements; the values of density ρ = 6486 kgm^{-3} for as-milled and ρ = 6463 kg m^{-3} for annealed samples were obtained from the Rietveld refinements of the XRD patterns; the values of thermal diffusivity α = 0.0774 × 10^{-4} m^{2}s^{-1} for the as-milled and 0.0660 × 10^{-4} m^{2}s^{-1} for annealed samples were obtained from the PAS measurements.

Considering the value of specific heat given in TAPP software [28] for the bulk SnTe phase (C_p = 211 J kg^{-1} K^{-1}), the thermal conductivity k ($k = \rho C_p \alpha$) was estimated and the calculated values were 10.59 Wm^{-1}K^{-1} for the as-milled and 9.00 Wm^{-1}K^{-1} for annealed samples. These values are slightly larger than that reported by Gelbestein[48] of k = 7.9 Wm $^{-1}$K^{-1} for bulk SnTe. Values of $\sqrt{Eg/K}$ = 0.0403 for the as-milled and 0.0480 for annealed samples were obtained. Zhang *et al.*[49] reported values of ZT ≈ 0.01 for the nanostructured undoped SnTe phase for temperatures smaller than 600 K and ZT ≈ 1.1 for the nanostructured $Sn_{1-x}In_xTe$ phase, with x = 0.25 at.%, for temperatures around 873 K. These values show that for applications of the SnTe phase as thermoelectric material, in addition to using crystallites of nanometric dimensions, it is also necessary to perform doping with pure elements and/or other phases to act as phonon spreading centers to reduce the thermal conductivity without promoting a strong degradation of the electrical properties. In this work, the presence of the SnO_2 and elemental Te phases in the as-milled and annealed SnTe samples did not reduce the thermal conductivity. The values of thermal conductivity of the SnO_2[59] and elemental Te phases are $k \approx 11$ Wm^{-1}K^{-1} and $k \approx 3$ Wm^{-1}K^{-1}, respectively.

A final comment: Poffo et al.[60] produced rhombohedral Bi_2Se_3 [space group R-3m (166)] using melting and mechanical alloying. They investigated the structural, optical and photoacoustic properties of the materials produced using the two methods and observed no significant differences.

5. Conclusions

A nanostructured SnTe phase was produced by MA. Using the Rietveld structural refinement procedure, the XRD patterns of as-milled and annealed samples were simulated. The α_{SnTe}^{CW} parameter showed that in the first coordination shell of SnTe there is a preference among the first neighbors for forming homopolar pairs. Probably due to this preference, the annealing process promoted a partial decomposition. This partial decomposition was corroborated by estimating the mean crystallite size using the Willianson-Hall plot corrected for a $pV(x)$ function used to represent the diffraction lines profiles, and relative volume fractions obtained from the Rietveld refinement procedure. The optical absorption measurements show that the band gap energy is inversely proportional to the crystallite size and follows an exponential law. Although the PAS analysis and the dimensionless figure of merit ZT for nanostructured SnTe showed that no significant advances relative to the results already reported in the literature were reached, the transport properties for the annealed nanostructured SnTe sample were determined.

6. Acknowledgments

One of authors (Z.V. Borges) thanks the Brazilian agency CNPq for financial support. We are indebted to the LABINC-UFSC for the optical transmittance measurements.

7. References

1. Schaller RD, Petruska M, Klimov VI. Tunable Near-Infrared Optical Gain and Amplified Spontaneous Emission Using PbSe Nanocrystals. *The Journal of Physical Chemistry B*. 2003;107(50):13765-13768.

2. Talapin DV, Murray C. PbSe nanocrystal solids for n- and p-channel thin film field-effect transistors. *Science*. 2005;310(5745):86-89.

3. Cao WY, Banin U. Growth and Properties of Semiconductor Core/Shell Nanocrystals with InAs Cores. *Journal of the American Chemistry Society*. 2000;122(40):9692-9702.

4. Lovett D. *Semi-Metals and Narrow-Bandgap Semiconductors*. London: Pion Limited; 1977.

5. Das VD, Bahulayan C. Variation of electrical transport properties and thermoelectric figure of merit with thickness in 1% excess Te-doped $Pb_{0.2}Sn_{0.8}Te$ thin films. *Semiconductor Science and Technology*. 1995;10(12):1638-1644.

6. Berger LI. *Semiconductor Materials*. Boca Raton: CRC Press; 1996.

7. Fürst J, Pascher H, Schwarz T, Böberl M, Heiss W, Springholz G, et al. Midinfrared IV-VI vertical-cavity surface-emitting lasers with zero-, two-, and three-dimensional systems in the active regions. *Applied Physics Letters*. 2002;81(2):208-210.

8. FIZ. *Inorganic Crystal Structure Database (ICSD)*. Kalrsruhe: Gmelin-Institute fur Anorganische Chemie and Fachinformationszentrum (FIZ); 1995.

9. Mengui UA, Abramof E, Rappl PHO, Ueta AY. Characterization of SnTe films grown by molecular beam epitaxy. *Brazilian Journal of Physics*. 2006;36(2A):324-327.

10. Sisman I, Öz H. Preparation of SnTe thin films on Au(111) by electrodeposition route. *Electrochimica Acta*. 2011;56(13):4889-4894.

11. An C, Tang K, Hai B, Shen G, Wang C, Qian I. Solution-phase synthesis of monodispersed SnTe nanocrystallites at room temperature. *Inorganic Chemistry Communications*. 2003; 6(2):181-184.

12. Saini R, Pallavi, Singh M, Kumar R, Jain G. Structural and electrical characterization of sintered SnTe films. *Chalcogenide Letters*. 2010;7(3):197-202.

13. Saini R, Singh M, Kumar R, Jain G. Electrical properties of $SnTe_xSe1-_x$ sintered films. *Optoelectronics and Advanced Materials - Rapid Communications*. 2009;3(1):49-52.

14. de Lima JC, Borba EC, Paduani C, dos Santos VHF, Grandi TA, Rechenberg HR, et al. Mechanical alloying of Fe and Zn: phase analysis and Mössbauer studies. *Journal of Alloys and Compounds*. 1996;234(1):43-47.

15. Weeber AW, Bakker H. Amorphization by ball milling. A review. *Physica B: Condensed Matter*. 1988;153(1-3):93-135.

16. Mukhopadhyay DK, Suryanarayana C, Froes HH. Extended solid solutions in Cd-Zn powders by mechanical alloying. *Scripta Metallurgica et Materialia*. 1994;30(1):133-137.

17. Yavari AR, Desré PJ, Benameur T. Mechanically driven alloying of immiscible elements. *Physical Review Letters*. 1992;68(14):2235-2238.

18. Che J, Yao X, Jian H, Wang M. Application and preparation of ZnSe nanometer powder by reduction process. *Ceramics International*. 2004;30(7):1935-1938.

19. Gleiter H. Materials with ultrafine microstructures: Retrospectives and perspectives. *Nanostructured Materials*. 1992;1(1):1-19.

20. Stern EA, Siegel RW, Newville M, Sanders PG, Haskel D. Are Nanophase Grain Boundaries Anomalous? *Physical Review Letters*. 1995;75(21):3874-3877.

21. Cullity BD. *Elements of X-Ray Diffraction*. 2nd ed. Reading: Addison-Wesley; 1978.

22. Young RA, ed. *The Rietveld Method. IUCr Monographs on Crystallography - 5*. Oxford: International Union of Crystallography/Oxford University Press; 1993.

23. Dasgupta P. On the intrinsic hook effect associated with pseudo-Voigt profiles. *Journal of Applied Crystallography*. 2002;35(Pt 2):267-269.

24. Rietveld HM. A Profile Refinement Method for Nuclear and Magnetic Structures. *Journal of Applied Crystallography*. 1969;2:65-71.

25. Larson AC, von Dreele RB. *General Structure Analysis System (GSAS)*. Report LAUR 86-748. Los Alamos: Los Alamos National Laboratory; 2004.

26. de Lima JC, Cella NL, Miranda LCM, An Chying C, Franzan AH, Leite NF. Photoacoustic characterization of chalcogenide glasses: Thermal diffusivity of Ge_xTe_{1-x}. *Physical Review B: Condensed Matter*. 1992;46(21):14186-14189.

27. Trichês DM, de Lima JC, Souza SM, Poffo CM, Grandi TA, de Biasi RS. Mechanical alloying of Co and Sb: Structural, thermal, optical, andphotoacoustic studies. *Journal of Applied Physics*. 2011;110(8):083528.

28. Microwave Inc. TAPP Software, *Version 2.2. E.S*. Wade Court: Microwave Inc.; 1998.

29. Maret M, Chieux P, Hicter P, Atzmon M, Johnson WL. Partial structure factors and chemical short-range order in $Ni_{33}Y_{67}$ and $Cu_{33}Y_{67}$ metallic glasses. *Journal of Physics F: Metal Physics*. 1987;17(2):315-333.

30. Atomic Softek. *Crystal Office 98 software*. Hamilton: Atomic Softek.

31. Sohn Y. Structural/Optical Properties and CO Oxidation Activities of SnO_2 Nanostructures. *Journal of the American Ceramic Society*. 2014;97(4):1303-1310.

32. Manzato L, Trichês DM, Souza SM, Oliveira MF. Synthesis of nanostructured SnO and SnO_2 by high-energy milling of Sn powder with stearic acid. *Journal of Materials Research*. 2014;29(1):84-89.

33. McLean TP. The Absorption Edge Spectrum of Semiconductors. In: Gibson AF, ed. *Progress in Semiconductors*. Vol 5. New York: John Wiley & Sons; 1960.

34. Boldish SI, White WB. Optical band gaps of selected ternary sulfide minerals. *American Mineralogist*. 1998;83:865-871.

35. Souza SM, Campos CEM, de Lima JC, Grandi TA, Pizani PS. Structural, thermal and optical studies of mechanical alloyed $Ga_{40}Se_{60}$ mixture. *Solid State Communications*. 2006;139(2):70-75.

36. Baltazar-Rodrigues J, de Lima JC, Campos CEM, Grandi TA. Effects of photoacoustic measurements on a nanostructured ZnSe mechanically alloyed. *Journal of Physics: Condensed Matter*. 2008;20(46):465205-465213.

37. Kovalenko MV, Heiss W, Shevchenko EV, Lee JS, Schwinghammer H, Alivisatos AP, et al. SnTe nanocrystals: A new example of narrow-gap semiconductor quantum dots. *Journal of the American Chemical Society*. 2007;129(37):11354-11355.

38. Xu Y, Al-Salim N, Hodgkiss JM, Tilley RD. Solution Synthesis and Optical Properties of SnTe Nanocrystals. *Crystal Growth & Design*. 2011;11(7):2721-2723.

39. Wang YY, Cai KF, Yao X. Facile synthesis and characterization of SnTe films. *Applied Surface Science*. 2011;258(2):919-922.

40. Aleksandrovsky A, Deshmukh VM, Fthenakis ZG. *Why do optical band gaps increase with decreasing size of nanomaterials?* Available from: https://www.researchgate.net/post/Why_do_optical_band_gaps_increase_with_decreasing_size_of_nanomaterials

41. Rosencwaig A, Gersho A. Theory of the photoacoustic effect with solids. *Journal of Applied Physics*. 1976;47(1):64-69.

42. Vargas H, Miranda LCM. Photoacoustic and related photothermal techniques. *Physics Reports*. 1988;161(2):43-101.

43. Pinto Neto A, Vargas H, Leite NF, Miranda LCM. Photoacoustic characterization of semiconductors: Transport properties and thermal diffusivity in GaAs and Si. *Physical Review B: Condensed Matter*. 1990;41(14):9971-9979.

44. de Lima JC, Schmitt M, de Souza SM, Almeida TO, Jerônimo AR, Trichês DM, et al. Structural and thermal study of nanostructured GaSb alloy prepared by mechanical alloying. *Journal of Alloys and Compounds*. 2007;436(1-2):13-18.

45. Trichês DM, Souza SM, de Lima JC, Grandi TA, Campos CEM. Structural and photoacoustic studies of Zn4Sb3 and ZnSb phases prepared by mechanical alloying. *Journal of Applied Physics*. 2009;105(6):063518.

46. Poffo CM, de Lima JC, Souza SM, Trichês DM, Grandi TA, de Biasi RS. Photoacoustic study of nanocrystalline silicon produced by mechanical grinding. *Physica B: Condensed Matter*. 2011;406(8):1627-1632.

47. Schmitt M, Poffo CM, de Lima JC, Fernandes CP, Santos VSS. Application of photoacoustic spectroscopy to characterize thermal diffusivity and porosity of caprocks. *Engineering Geology*. 2017;220:183-195.

48. Gelbstein Y. Thermoelectric power and structural properties in two-phase Sn/SnTe alloys. *Journal of Applied Physics*. 2009;105(2):023713.

49. Zhang Q, Liao B, Lan Y, Lukas K, Esfarjani W, Opeil C, et al. High thermoelectric performance by resonant dopant indium in nanostructured SnTe. *Proceedings of the National Academy of the United States of America (PNAS)*. 2013;110(33):13261-13266.

50. Rousset G, Lepoutre F, Bertrand L. Influence of thermoelastic bending on photoacoustic experiments related to measurements of thermal diffusivity of metals. *Journal of Applied Physics*. 1983;54(5):2383-2391.

51. Dramicanin MD, Nikolic PM, Ristovski ZD, Vasiljevic DG, Todorovic DM. Photoacoustic investigation of transport in semiconductors: Theoretical and experimental study of a Ge single crystal. *Physical Review B: Condensed Matter*. 1995;51(20):14226-14233.

52. Lichtenecker K. Die Dielektrizitätskonstante künstlicher und natürlicher Mischkörper. *Physikalische Zeitschrift*. 1926;27:115-158.

53. Simpkin R. Derivation of Lichtenecker's; logarithmic mixture formula from Maxwell's equations. *IEEE Transactions on Microwave Theory and Techniques*. 2010;58(3):545-550.

54. ChemGlobe. *Periodic Table of the Elements*. Available from: <http://pol.spurious.biz/projects/chemglobe/ptoe/>. Access in: 26/4/2018.

55. Turkes P, Pluntket C, Helbig R. Thermal conductivity of SnO_2 single crystals. *Journal of Physics C: Solid State Physics*. 1980;13(26):4941-4951.

56. Rowe DM, Shukla VS. The effect of phonon-grain boundary scattering on the lattice thermal conductivity and thermoelectric conversion efficiency of heavily doped fine-grained, hot-pressed silicon germanium alloy. *Journal of Applied Physics*. 1981;52(12):7421-7426.

57. Ur SC, Nash P, Kim IH. Mechanical alloying and thermoelectric properties of Zn_4Sb_3. *Journal of Materials Science*. 2003;38(17):3553-3558.

58. Tripathi MN, Bhandari CM. Material parameters for thermoelectric performance. *Pramana*. 2005;65(3):469-479.

59. Shi L, Hao Q, Yu C, Mingo N, Kong X, Wang ZL. Thermal conductivities of individual tin dioxide nanobelts. *Applied Physics Letters*. 2004;84(14):2638-2640.

60. Poffo CM, de Lima JC, Souza SM, Trichês DM, Nogueira TPO, Borges ZV, et al. Structural, optical and photoacoustic study of milled and melted Bi_2Se_3. *Journal of Molecular Structure*. 2014;1076:737-742.